



HAL
open science

Aluminum based metal-organic framework integrated with reduced graphene oxide for improved supercapacitive performance

Mandira Majumder, Ram Choudhary, Anukul Thakur, Ali Khodayari, Mandana Amiri, Rabah Boukherroub, Sabine Szunerits

► To cite this version:

Mandira Majumder, Ram Choudhary, Anukul Thakur, Ali Khodayari, Mandana Amiri, et al.. Aluminum based metal-organic framework integrated with reduced graphene oxide for improved supercapacitive performance. *Electrochimica Acta*, 2020, 353, pp.136609. 10.1016/j.electacta.2020.136609 . hal-03090009

HAL Id: hal-03090009

<https://hal.science/hal-03090009>

Submitted on 21 Jun 2022

HAL is a multi-disciplinary open access archive for the deposit and dissemination of scientific research documents, whether they are published or not. The documents may come from teaching and research institutions in France or abroad, or from public or private research centers.

L'archive ouverte pluridisciplinaire **HAL**, est destinée au dépôt et à la diffusion de documents scientifiques de niveau recherche, publiés ou non, émanant des établissements d'enseignement et de recherche français ou étrangers, des laboratoires publics ou privés.



Distributed under a Creative Commons Attribution - NonCommercial 4.0 International License

Aluminum based metal-organic framework integrated with reduced graphene oxide for improved supercapacitive performance

Mandira Majumder^{a,b}, Ram B. Choudhary^{b,}, Anukul K. Thakur^b, Ali Khodayari^c, Mandana Amiri^c, Rabah Boukherroub^a, Sabine Szunerits^{a,*}*

^aUniv. Lille, CNRS, Centrale Lille, Univ. Polytechnique Hauts-de-France, UMR 8520 - IEMN, F-59000 Lille, France.

^bNanostructured Composite Materials Laboratory, Department of Physics, Indian Institute of Technology (Indian School of Mines), Dhanbad, Dhanbad 826004, India.

^cDepartment of Chemistry, University of Mohaghegh Ardabili, Ardabil, Iran.

Corresponding Authors

* e-mail: rbcism@gmail.com
Tél : +91 (0) 326 223 5881

* e-mail: sabine.szunerits@univ-lille.fr
Tél : +33 (0)3 62 53 17 25
Fax : +33 (0)3 62 53 17 01

ABSTRACT

Integration of aluminum-terephthalate metal-organic framework, MIL-53 (Al) with reduced graphene oxide (rGO) leads to the formation of hybrid materials with superior charge storage properties. This work reports the synthesis of MIL-53 (Al) integrated with rGO through solvothermal method and study of their electrochemical charge storage properties. The optimized composite of MIL-53 (Al) and rGO (coded as C-10) exhibits a specific capacitance of 280 F g^{-1} at 0.5 A g^{-1} . Furthermore, electrochemical measurements, carried out in a symmetric two-electrode configuration, revealed that the hybrid composite C-10 reached an energy density of 6.66 Wh kg^{-1} and a power density of 3655 W kg^{-1} . It displayed a capacitance retention of 50% after 5,000 charge/discharge cycles. Integration of MIL-53(Al) and rGO leads to the creation of alternate pathways for ion-diffusion, hierarchical pore features, greater exposure of MIL-53 (Al) clusters as redox active sites attributed to their uniform distribution on rGO sheets, resulting in better charge storage performance.

KEYWORDS. Metal-Organic Frameworks; MIL-53 (Al); Reduced Graphene Oxide; Nanocomposites; Supercapacitor.

1. Introduction

Energy storage systems capable of delivering high energy density at fast charge/discharge rates have become a necessity for future portable devices. Supercapacitors (SCs) are currently one of the most promising candidates for next-generation power devices characterized by excellent power density, fast charge/discharge rates, and long life span [1]. The low capacitance of most SCs is however not compatible with systems where large energy density is required. The key factor influencing the performance of a SC device is the electrode material.

Carbon-based SCs are known as pioneering electrode materials for commercial electrochemical double layer (EDL) supercapacitors [2]. Reduced graphene oxide (rGO) is largely preferred as EDL capacitive material, owing to its unique properties such as high electrical conductivity [3], good cyclic stability [4], and ultra-high specific surface area [5]. However, rGO faces the problem of intense agglomeration that limits the active surface available for interaction with the electrolyte, limiting its specific capacitance and energy density [6].

An attractive way to mitigate this limitation is to introduce pseudocapacitive materials like conducting polymers (polyaniline, polypyrrole, polythiophene, poly-N-phenylglycine, and polyindole), metal oxides, nitrides, sulphides, and MXenes where fast redox reactions occur near the electrode surfaces [2, 7, 8]. However, the low electrical conductivity (10^{-5} to 10^{-6} S cm^{-1}) of metal oxides and nitrides [9], the low interlayer conductivity of two-dimensional metal sulphides (e.g. MoS_2) [10], together with agglomeration problems and instability of the backbone of conducting polymers [11], are limiting the widespread use of these materials in SCs.

A newly emerging class of materials seeking attention for application in electrochemical energy storage systems is metal organic frameworks (MOFs) [12]. MOFs are organic-inorganic hybrid crystalline porous materials consisting of a regular array of positively charged metal ions surrounded by organic linker molecules [12]. MOFs are promising electrode materials, because of their various modular and controllable structures as well as tunable specific surface area and internal pore volume [13]. MOFs are thus garnering more and more attention as one of the best promising materials for energy storage devices. MOFs in pristine form are redox active, owing to the presence of metal cations, imparting pseudocapacitance property [14]. The highly reversible redox reactions usually take place at the surface and/or near the surface of redox-active sites [14]. More than a handful of different MOFs based on zinc, nickel, cobalt, manganese, iron etc. have been reported for SC applications [15]. For the first time, Diaz et al. reported on the use of MOF Co8-MOF-5 ($\text{Zn}_{3.68}\text{Co}_{0.32}\text{O}(\text{BDC})_3(\text{DEF})_{0.75}$) as an electrode material for SC. The electrode material exhibited a specific capacitance of 0.30 F g^{-1} at 10 mA g^{-1} with 8% decrease in the specific capacitance value after 1,000 galvanostatic charge/discharge cycles in 0.1 M tetrabutylammonium hexafluorophosphate dissolved in acetonitrile [16]. Co-based conducting MOF as reported by Yang et al. [17] achieved a specific capacitance as high as 2564 F g^{-1} at 1 A g^{-1} in 5 M KOH with an excellent capacitance retention of 95.8% after 3,000 cycles. However, scaling up production and very low electrical conductivity remain a major concern for the application of pristine MOFs as supercapacitor electrode materials [18, 19]. In addition, the structural instability of MOFs in pristine form in aqueous media significantly restricts their use in energy storage devices employing aqueous electrolytes [18,19].

MOFs are commonly used as precursors for the synthesis of porous carbon for supercapacitor applications with improved stability and conductivity [20, 21]. As reported by Jiang and co-

workers, nitrogen-doped porous carbon derived from Al-based MOF displays a specific capacitance of 332 F g^{-1} at 1 A g^{-1} with a capacitance retention of 97.8% after 100,000 charging/discharging cycles [20]. In another work, they reported a specific capacitance of 318.7 F g^{-1} at 1 A g^{-1} showing good cyclic stability with 96.4% capacitance retention at a current density of 100 A g^{-1} after 50,000 cycles [21]. However, carbonization of MOFs needs high temperature and involves large amount of energy, which may not be feasible always. Hence, it is necessary to develop structurally stable MOFs and strategies to improve their electrical conductivity which can serve aptly as electrode materials for SCs. Aluminum (Al)-based MOFs have shown promising aspects in connection to energy storage applications due to involvement of inexpensive and non-poisonous metal precursors, resulting in high mechanical and chemical stability [22, 23]. Solvothermally synthesized MIL-53 (Al), consisting of numerous *trans* strands of corner sharing $\text{AlO}_4(\text{OH})_2$ octahedra interconnected by 1,4-benzenedicarboxylate ligands, is of particular interest for electrochemical energy storage due to its exceptional structural stability in aqueous media. According to a chemical stability study conducted by Qian et al., MIL-53 (Al) showed exceptional structural stability in basic (pH=14) aqueous solution, which is better than all the known MOFs and is inferior to only $\text{Ni}_2(\text{BTP})_2$ framework [24]. The outstanding stability of pristine MIL-53 (Al) is mainly credited to the strong chemical bonding persisting between Al-atoms from the metal clusters and the oxygen atoms. Furthermore, the hydrophobic property of the aromatic boundaries results in repulsion of the water molecules, hindering the attack on the $\text{AlO}_4(\text{OH})_2$ octahedral units hence preventing disintegration of the framework. These two combined features can be credited to the enhanced structural stability of pristine MIL-53 (Al) in aqueous solutions [24].

In this work, we report on the preparation of pristine MIL-53 (Al), an aluminum-based MOF derived from aluminum nitrate as metal precursor and benzene-1,4-dicarboxylic acid (BDC) as organic linker, by a solvothermal approach. BDC was used as the organic linker due to its

excellent binding ability with Al^{3+} as compared to the other organic linkers [13], and its low solubility in aqueous medium (0.0017 g per 100 mL at 25 °C), but excellent solubility in DMF [25]. MIL-53 (Al) was integrated with reduced graphene oxide (rGO) nanosheets to increase the conductivity of the hybrid matrix and limit rGO aggregation. The performance of MIL-53 (Al)@rGO, coded as C-2, C-5, C-10, C-20, and C-50 according to the weight (wt. %) of rGO, as supercapacitor electrodes was evaluated in 1 M KOH solution. It was found that integration of rGO into MIL-53 (Al) helped to improve the double layer charge storage, electrolytic ion transport, and active surface area exposed for electrode-electrolyte interactions. All these together resulted in better specific capacitance of the optimized hybrid-composite as compared to both rGO and pristine MIL-53 (Al), taken separately.

2. Experimental section

2.1 Materials

1,4- benzene dicarboxylic acid (BDC, 97%), N, N-dimethylformamide (DMF, 99.8%), aluminum nitrate nonahydrate ($\text{Al}(\text{NO}_3)_3 \cdot 9\text{H}_2\text{O}$, 99.99%), potassium hydroxide (KOH, >86%), carbon black (>99.95%), N-methyl-2-pyrrolidone (NMP, 99.5%), reduced graphene oxide (rGO) and poly(vinylidene fluoride) were procured from Sigma-Aldrich. All the chemicals were used as received without any further purification. Deionized (DI) water was used for all the experimental purposes.

2.2. Synthesis of MIL-53 (Al) MOF (C-1)

Aluminum nitrate nonahydrate (0.166 g, 1 mmol) and benzene-1,4-dicarboxylic acid (0.75 g, 2 mmol) were mixed in a molar ratio of 1:0.5 in 50 mL DMF, as reported previously [26]. This mixture was then ultrasonicated for 30 min to attain homogeneity and was transferred into a 125 mL Teflon-lined autoclave. The autoclave was placed in an oven maintained at 120 °C for 48 h. After the reaction was completed, the obtained mixture was centrifuged at 4400

rpm for 40 min. Thereafter, the precipitate was washed with DMF three times and dried at room temperature under the fume-hood.

2.3. Preparation of MIL-53 (Al)@rGO nanocomposites (C-2, C-5, C-10, C-20, and C-50)

Reduced graphene oxide (rGO) was solvothermally integrated with MIL-53 (Al) *ex-situ*, using DMF as the solvent in a 125 mL Teflon-lined autoclave. For the synthesis of C-2 composite, 0.25 g of MIL-53 (Al) was mixed with 0.005 g of rGO in 50 mL of DMF and ultrasonicated till formation of a homogeneous solution. The solution was then transferred into a 125 mL Teflon-lined autoclave and heated at 120° C for 24 h. The obtained solution was centrifuged at 4400 rpm and the precipitate was washed three times with DMF and dried at room temperature. The other composites C-5 (5 wt. % rGO), C-10 (10 wt. % rGO), C-20 (20 wt. % rGO), and C-50 (50 wt. % rGO) were synthesized by varying the content of rGO. Here onwards in the manuscript we would use the term C-1 for pristine MOF MIL-53(Al) and C-100 for pristine rGO.

2.4 Characterization Methods

The crystallinity of the as-prepared materials was assessed by X-ray diffraction (XRD) technique in the 2θ range from 5° to 40° using XPERT-PRO Cu-K α radiation. Raman spectroscopic technique (T64000, Jobin Yvon Horiba, France) was used to characterize the as-prepared materials in the 200-2000 cm⁻¹ wavenumber range. The bonding and chemical structure of the as-synthesized materials were characterized using Fourier transform infrared (FTIR) spectroscopy technique (Bruker Vertex 80v) in the 4000-700 cm⁻¹ wavenumber range. Sample preparation involved mixing the electrode material with KBr in a ratio of 1:20 in an agate mortar followed by pressing them in thin pellets by applying a pressure of 5 tons for 7 min. X-ray photoelectron spectroscopy (XPS) analysis was performed on PHI 5000 Versa Probe II spectrometer at 5 \times 10⁻¹¹ Torr. The morphology of the composites was examined

using field emission scanning electron microscopy (FESEM) (Supra-55 Carl ZEISS Germany) technique at an accelerating voltage of 5 kV and vacuum of 10^{-4} - 10^{-6} mm Hg. High resolution transmission electron microscopic (HR-TEM) images were recorded using JEM 2100F JEOL, Tokyo, Japan, electron microscope operating at 200 kV. The sample was dispersed in ethanol through ultrasonication for 1 h. Then the dispersion was drop-casted on carbon coated copper grid followed by drying overnight at 70°C. Surface area and pore size distribution of the as-prepared materials were analyzed using 3FLEX 3500, Micrometrics Instrument Corporation, USA, gas sorption analyzer using liquid nitrogen at 77 K. Adsorption-desorption isotherms were recorded to obtain the surface area using Brunauer-Emmett-Teller (BET) method and pore size distribution using Barrett- Joyner-Halenda (BJH) model.

2.5. Electrochemical tests

Electrochemical measurements were performed on PGSTAT Metrohm Autolab instrument equipped with a frequency response analyzer FRA in 1 M KOH (pH =14) as the electrolyte. For the three-electrode configuration, Ag/AgCl was used as the reference electrode, and a platinum plate was used as the counter electrode. For the preparation of the working electrodes, the synthesized sample (1.7 mg), carbon black (0.2 mg) as the conducting agent, and polyvinyl difluoride (PVDF) (0.1 mg) (wt. ratio of 85:10:5) were mixed in an agate mortar. A slurry of the powder mixture (2 mg) was made by adding NMP (100 μ L) and thoroughly mixing it in an agate mortar. The slurry was then coated on Ni-foam current collector within an area of 1 cm² and dried at 70 °C overnight.

Cyclic voltammetry (CV) measurements were performed by varying the scan rate from 10 to 200 mV s⁻¹ (10, 20, 50, 100, and 200 mV s⁻¹).

Galvanostatic charging-discharging measurements (GCD) were acquired by varying the current density from 0.5 to 10 A g⁻¹ (0.5, 1, 2, 3, 5, and 10 A g⁻¹). Electrochemical impedance

spectroscopic (EIS) measurements were performed in the 100 kHz-0.1 Hz frequency range. To allow sufficient time for the electrolyte to penetrate the pores of the electrode materials, each synthesized material was soaked in the electrolyte i.e. 1 M KOH for 120 min prior to the EIS measurements. Furthermore, each sample was also cycled at a low scan rate of 10 mV s⁻¹ for 5 cycles to improve the stability [27, 28].

The specific capacitance (C_s) for the electrode materials was calculated using equation (1) [29]:

$$C_s = \frac{I\Delta t}{m\Delta V} \quad (1)$$

where I is the applied current (mA), Δt the discharging time (s), ΔV the potential window (iV), and m the mass loading (mg).

Further, to assess the true performance of the electrodes, electrochemical measurements were conducted in a symmetric two-electrode configuration. The coulombic efficiencies of the electrode materials at 3 A g⁻¹ were calculated according to equation (2) [30]:

$$\eta = \frac{t_d}{t_c} * 100 \quad (2)$$

where t_d is the discharge time and t_c is the charging time expressed in s. The energy density and power density of the electrode materials at various current densities are calculated using equations (3-4) [29]:

$$E = \frac{1}{2} C \Delta V^2 \frac{1000}{3600} \quad (3)$$

$$P = E / \Delta t \quad (4)$$

where C is the specific capacitance obtained for the two-electrode system (F g⁻¹), ΔV is the potential window (V), and Δt is the discharging time (h).

3. Results and Discussion

3.1. Characterization of MIL-53 (Al) and MIL-53 (Al)@rGO

The synthesis of MIL-53 (Al) (C-1) is schematically illustrated in [Figure 1](#). The preparation of MIL-53 (Al)@rGO hybrid composites is achieved using a two-step reaction: solvothermal synthesis of C-1, followed by solvothermal integration into rGO. The morphologies of the different hybrid materials (C-1, C-2, C-5, C-10, C-20, C-50, C-100) as seen from the FE-SEM images are depicted in [Figure 2](#). The composition of these composites is listed in **Table 1**. The FE-SEM image of C-1 MOF shows nanoscale features with typical MOF cluster size lying within 100 nm [\[31\]](#). The C-100 (pristine rGO) displays stacked sheets with numerous ripped features. These ruptures existing in the surface of the C-100 sheets are also visible in the other hybrid composites containing rGO viz., C-2, C-5, C-10, C-20, and C-50. It is believed that these small openings on the rGO surface would lead to seeping of electrolyte into the interiors of the electrode materials, leading to better access of the electrode active sites by the electrolyte. Further, as can be seen in the SEM images of C-1 ([Figure 2A](#)) and C-100 ([Figure 2I](#)), both these parent materials face agglomeration and stacking. In C-100 (rGO), the stacking of the sheets is very clearly visible, while in case of the C-1 (MIL-53 (Al)) the clusters are densely packed. For the hybrid composites, the stacking of the rGO sheets is limited by the intervening MIL-53 (Al) clusters. Also, the MIL-53 (Al) clusters are distributed on the rGO sheets, limiting their intense agglomeration. Hence, both rGO and MIL-53 (Al) participate synergistically in reducing the agglomeration and stacking, leading to exposure of larger electrode active surface. FE-SEM images of the MIL-53 (Al)@rGO matrices revealed that the density of MIL-53 (Al) clusters increases with a decrease in the rGO content ([Figure 2B-H](#)).

Using C-10 as example, HR-TEM images (**Figure S1**) revealed light grey shaded sheet like features representing the rGO sheets and small nano-scaled irregular clusters of MIL-53 (Al) MOFs, indicated by the blue arrows. These images clearly indicate the formation of

nanosized clusters of MIL-53 (Al) MOFs and their successful integration within the rGO sheets.

The XRD pattern of C-100 (pristine rGO) consists of a broad peak centered at around $2\theta=24^\circ$ (Figure 3A), revealing the amorphous nature of rGO in accordance with literature reports [32]. The XRD pattern of C-1, MIL-53 (Al), displays bands at $2\theta=10.14^\circ$, 15.44° , 21.04° , and 27.6° corresponding respectively to the (200), (011), (302), and (020) hkl planes, matching well with the previously reported XRD patterns of MIL-53 (Al) [25, 33]. The XRD patterns of the MIL-53 (Al)@rGO nanocomposites (Figure 3A) clearly show the diffraction bands of C-1. An increase in the rGO content in the hybrid composite results in a decrease of the C-1 bands intensities.

Raman spectroscopy was thus further used (Figure 3B) to validate the presence of rGO in the hybrid structures. The Raman spectrum of MIL-53 (Al) depicts bands at 1615 cm^{-1} (C=C ring stretching) [34], 1473 cm^{-1} (symmetric stretching of COO^-) [34] and 1150 and 872 cm^{-1} assigned to the deformation of aromatic C-H [34]. Another peak at 631 cm^{-1} is attributed to the presence of aromatic ring deformation [34]. The Raman spectrum of C-100 (rGO) comprises two intense peaks centered at around 1360 and 1588 cm^{-1} characteristic of the D- and G-bands for the sp^3 and sp^2 hybridized carbon atoms, respectively [32]. The G-band for the sp^2 hybridized carbons is ascribed to the E_g^2 phonons at the middle of the Brillouin zone [32]. The D-band for the sp^3 carbons is attributed to the existence of the breathing mode due to the presence of defects in the skeleton [32]. The Raman spectra of the nanocomposites consist of the characteristic bands of C-1 and C-100, with a decrease in the G-band of rGO with increasing the amount of C-1.

The chemical bondings of MIL-53 (Al) and MIL-53 (Al)@rGO were evaluated by FTIR (Figure 3C). The FTIR spectrum of C-1 displays a broad vibration band centered at 3432 cm^{-1}

mainly attributed to the hydroxyl group stretching present in the MOF system [35]. The vibration of the COO^- group of the organic linker occurs between $1700\text{-}1400\text{ cm}^{-1}$ [33]. The vibration peaks at 1613 and 1510 cm^{-1} are assigned to asymmetric stretching of -COO^- group, while the bands at 1442 and 1409 cm^{-1} are ascribed to the symmetric stretching of -COO^- group. These values match well with FTIR literature data for -COO^- originating from the BDC organic linker coordinated to Al-metal centers in $\text{AlO}_4(\text{OH})_2$ octahedra [33, 36]. The appearance of these symmetric and asymmetric stretching bands of the -COO^- groups coordinated to the Al-metal centers elucidates the structure of MIL-53 (Al) MOF more clearly. As can be seen in the Figure 3D, in C-1 i.e., MIL-53 (Al) MOF, the Al-metal centers form $\text{AlO}_4(\text{OH})_2$ octahedra, where one Al-atom is coordinated to four oxygen atoms belonging to four different -COO^- groups of the BDC linkers [37]. The other two oxygen atoms coordinated to the Al-atom come from the -OH groups linking the neighboring Al-metal centers [37]. For more clarity, the H-atoms have been omitted from the structures. As can be seen in the Figure 3E, the -COO^- groups of the BDC linkers, coordinated to the Al-metal centers, undergo asymmetric and symmetric stretching vibrations giving rise to the corresponding FTIR bands, as stated earlier [37, 38]. Furthermore, it is worth mentioning that MIL-53 (Al) MOF contains rigid parts, including the aromatic rings and less rigid chains of Al-octahedra [39]. Nevertheless, owing to the flexibility of the Al-O and C-O bonds, the linkage between the Al-octahedra and the -COO^- is flexible, and the organic linker can rotate around the O-O axis [40]. Hence, the BDC-Al-BDC angle can vary largely [39]. This phenomenon imparts a very significant property to the MIL-53 (Al) MOF, which is popularly termed as “breathing effect” [40]. Credited to this effect, these MOFs can accommodate guest molecules effectively within their large pores, widening their applications in gas adsorption and storage [40]. The peak at 1677 cm^{-1} is ascribed to the stretching vibration of the carbonyl groups belonging to the uncoordinated organic linker BDC trapped within the MIL-53 (Al)

pores [37,36]. As can be seen in the Figure 3F, these residual organic linkers simply reside within the pores of the MIL-53 (Al) framework and do not form any coordination bonds with the Al-metal clusters of the $\text{AlO}_4(\text{OH})_2$ octahedra [37, 41]. Hence, these trapped BDC are not directly involved in forming the MIL-53 (Al) framework. The peak ranging from 800-700 cm^{-1} is attributed to the lattice vibrations of C-H bond of MIL-53 (Al) [33]. The FTIR spectrum of rGO (C-100) depicts bands at 1734, 1560, and 1215 cm^{-1} ascribed to the stretching of -COOH groups, graphitic carbons, and epoxy symmetric ring deformation, respectively [35]. In the FTIR spectra of C-2, C-5, C-10, C-20, and C-50 composites, the peaks of rGO are less visible.

In addition, XPS analysis (Figure 4) was carried out to gain further information on the elemental composition and bonding states in the synthesized materials. The XPS wide scan of the C-10 hybrid composite (Figure 4A) reveals the presence of C_{1s} (285 eV), O_{1s} (531 eV), Al_{2s} (73 eV), and Al_{2p} (120 eV). The high-resolution spectra of C_{1s} , O_{1s} , Al_{2s} , and Al_{2p} of C-10 hybrid composite are displayed in Figures 4(B-E). The XPS high resolution spectrum of the C_{1s} can be deconvoluted into peaks at 284.4 eV (C=C), 285 eV (C-C/C-H), 286.7 eV (C-O), 288.0 eV (COO^-), 289 eV (C=O/O-C=O), and 291.2 eV ($\pi-\pi^*$ bonds), as shown in Figure 4B [42-44]. The O_{1s} peak could be deconvoluted into four peaks appearing at 531.1 eV (C=O), 531.7 eV ($\text{AlO}_4(\text{OH})_2$ in the octahedral geometry formed as a result of the association of the Al centers in C-1), 532.5 eV (C-O), and 531.9 eV (O-C=O), as shown in the Figure 4C [42-44]. The Al_{2p} peak is curve-fitted with two components (Figure 4E); one of the deconvoluted peaks at 73.2 eV is attributed to the residual tetrahedral Al formed unintentionally during the synthesis and the other major peak at 75.2 eV is assigned to the Al^{3+} in octahedral frames of $\text{AlO}_4(\text{OH})_2$ clusters linked to the organic linker forming MIL-53 (Al) MOF [43, 45].

N_2 adsorption-desorption isotherms are depicted in [Figure 5](#). The isotherms are type IV curves with the presence of hysteresis loops, indicating multilayer adsorption followed by capillary condensation ([Figure 5A](#)) [46]. The small intake in the low relative pressure region ($P/P_0 \sim 0.01$) suggests the presence of micropores [46]. For C-100 (rGO), the hysteresis loop is identified as of H3-type originating from the aggregates of C-100 sheets forming slit-like pores [46]. For the C-10 hybrid composite and C-1, the hysteresis loops are identified as of H2-type, pointing towards the presence of pores with narrow openings (ink-bottle pore types) [46]. The Brunauer–Emmett–Teller (BET) surface area is $1.989 \text{ m}^2 \text{ g}^{-1}$ for C-100. For C-1 it is $144 \text{ m}^2 \text{ g}^{-1}$ and increased to $256 \text{ m}^2 \text{ g}^{-1}$ (1.8 times) with the incorporation of rGO in C-10 hybrid composite. The surface area obtained for the C-100 was larger than $900 \text{ m}^2 \text{ g}^{-1}$ reported by Ossoon et al. [5]. Nevertheless, the value of the specific surface area of C-1 is much lower as compared to the activated MOF system reported previously ($1013 \text{ m}^2 \text{ g}^{-1}$) by Rahmani et al. [47]. The pore width distributions in the electrode materials were obtained using Barrett-Joyner-Halenda (BJH) model ([Figure 5B](#)). For C-100, a clear mesopore dominance (pink shaded region) with the presence of a few micropores (yellow shaded region) can be seen. The average diameter of C-100 is 21.7 nm. In case of C-1, the average pore diameter was determined to be 18.1 nm, which decreased to 17.8 nm for the C-10 hybrid composite. As can be seen in [Figure 5B](#), the number of micropores increases for the C-10 hybrid composite as compared to C-1. This can be explained by the fact that as a result of incorporation of rGO into MIL-53 (Al), mesopores are converted into micropores (smaller pores) resulting in a decrease in the average pore width. Since smaller pores usually contribute more to specific surface area as compared to larger pores, incorporation of rGO into MIL-53 (Al) leads to increase in the specific surface area in the C-10 hybrid composite.

3.2. Electrochemical analysis of MIL-53 (Al) and MIL-53 (Al)@rGO

Electrochemical analysis of C-1 (MIL-53 (Al)), C-100 (rGO) and MIL-53(Al)@rGO hybrid composites (C-2 to C-50) electrodes were conducted in 1 M KOH aqueous electrolyte. All CVs plots show a scan-rate dependent response (Figure 6A and Figure S2) attributed to the variation in the thickness of the diffusion layer formed at the interface of the electrode active material and the electrolyte, in turn altering the interaction and hence the current response. CV curves obtained for C-1 (MIL-53 (Al)) deviate significantly from the ideal rectangular behavior, indicating pseudocapacitive property (quasi-reversible reaction characteristics) of the material, owing to the redox reaction of Al (attributed to multiple valence states) from the MIL-53 (Al) with the electrolyte (Figure S2A) [48]. CV curves recorded for C-100 (rGO) are more rectangular in nature without any observable redox peak, indicating EDL capacitance prevalence (Figure S2B). For the composite materials (Figure 6A and Figure S2(C-F)), the degree of rectangularity and intensity of the redox peaks varied with the content of rGO and MIL-53 (Al). For C-10 hybrid composite, the redox peaks (at -0.159 V for oxidation and at -0.519 V for reduction) are clearly observed at a low scan rate of 10 mV s^{-1} , as represented in Figure 6A (inset), indicating the main contribution of redox charge storage from the MOF. Since, the area under the CV curves obtained at the same scan rate is directly related to the specific capacitance, the comparison of the CV curves at a fixed scan rate of 200 mV s^{-1} (Figure 6B) reveals that the best capacitive performance is exhibited by the C-10 hybrid composite electrode material.

Galvanostatic charge/discharge cycling is shown in Figure 6C for C-10 (for other electrodes, see Figure S3(A-F)) by varying the current density from 0.5 to 10 A g^{-1} . Charging/discharging time increases with a decrease of the current density. The comparative charging/discharging plots in Figure 6D clearly indicates that the charging and discharging times are the longest for the C-10 hybrid composite. The redox peaks seen in the CV plots for the C-10 hybrid composite (Figure 6A) (more clearly seen at the lower scan rate of 10 mV s^{-1}

as represented in the inset of Figure 6A) suggest a contribution of faradaic capacitance. In fact, the charge storage proceeds through dual contribution from surface-controlled (EDL) and diffusion-related charge components (pseudocapacitance) in C-10 hybrid composite. Hence, the total voltammetric charge stored (q_T) can be expressed as a combination of charge stored from “inner (q_i)” less accessible surface and “outer (q_o)” more exposed and accessible surface of the electrode material. The contribution of charge storage from both these components was calculated using previously reported methods (Eqs. 5, 6) [49, 50]. The surface charge (q_o) mainly comes from outer electrochemical surface interaction of the electrode active material and electrolyte, depending essentially on the region of direct contact between the electrolyte and the electrode. On the other hand, the inner charge (q_i) arises essentially from the grain boundaries voids, dislocations, pores, cracks and crevices etc. from the inner region of the electrode material. The participation of the inner diffusion-controlled sites in charge storage is dependent on the scan rate (ν) and becomes inactive with increasing the scan rate. The equations (5-6) representing these behaviors are [50]:

$$\frac{1}{q(\nu)} = \frac{1}{q_T} + \text{const}'(\sqrt{\nu}) \quad (5)$$

$$q(\nu) = q_o + \text{const}\left(\frac{1}{\sqrt{\nu}}\right) \quad (6)$$

The total charge (q_T) due to the outer and inner charge components can be assessed by extrapolating the linear region of the graph of ‘ $q(\nu)^{-1}$ ’ versus ‘scan rate^{1/2}’, (Figure 6E) to obtain the y-intercept where the x-axis value i.e. the ‘scan rate’ goes to zero. At this point, we assume the full participation of the inner as well as the outer charge storing components [50]. On the other hand, ‘ q_o ’ can be calculated from extrapolation of the ‘ $q(\nu)$ ’ versus ‘scan rate^{-1/2}’, plot (Figure 6F), assuming that as the scan rate tends to infinite the diffusion driven charge storage is completely seized [50]. Then, the contribution of the ‘ q_i ’ can be easily calculated by subtracting ‘ q_o ’ from ‘ q_T ’. The estimated contribution from the inner and outer charge

components strongly suggests the dominance of reversible redox reactions (88%) to the high specific capacitance of C-10 electrode. This can be attributed to the enhanced porosity in case of the C-10 composite and modified morphology creating alternation paths for ion diffusion. Also, integration of rGO limits the aggregation caused in the MIL-53 (Al) MOF clusters exposing more active sites, which can interact with the electrolyte and enhance the charge storage properties of the C-10 hybrid composite.

The specific capacitance of the electrode materials is represented graphically in [Figure 7A](#). The specific capacitance of C-1 is 6.5 F g^{-1} (0.5 A g^{-1}) due to the low electrical conductivity of C-1 and its agglomeration [\[51\]](#). Also, intense agglomeration of C-1 inhibits the electrolytic ions to access the inner active sites (major portion of the charge storage in C-1 comes from pseudocapacitance), severely limiting its specific capacitance [\[16\]](#). In the case of C-100, a $C_s = 212 \text{ F g}^{-1}$ at 0.5 A g^{-1} was determined and decreases to 87 F g^{-1} at 10 A g^{-1} . The specific capacitance scales with the amount of rGO in the nanocomposite: C-2 exhibits a specific capacitance of 52 F g^{-1} at 0.5 A g^{-1} and increases to 140 F g^{-1} for the C-5 with the highest specific capacitance of 280 F g^{-1} for C-10. Further increasing the amount of rGO in the nanocomposite decreases C_s to 268 F g^{-1} (C-20) and 235 F g^{-1} (C-50).

The trend of the variation in the specific capacitance at a fixed current density of 0.5 A g^{-1} of the electrode materials with varying content of rGO is graphically represented in [Figure 7B](#). The initial increment in the value of specific capacitance as the content of rGO increases from 2-10 wt.% is attributed to increase in the conductivity by the modified morphology, introducing more pores and hence enhanced specific surface area. However, there is a reduction in the value of specific capacitance as the content of rGO is further increased to 50 wt.%, which is ascribed to reduction in bulk storage of specific capacitance and loss of active sites. This leads to setting up an optimum for the C-10 composite with 10 wt.% of rGO where the maximum synergy is established. The value of specific capacitance of C-10 composite

exceeds that of pristine rGO (C-100), which is indicative that the resulting specific capacitance is not just a sum of the contributions of C-1 (MIL-53 (Al)) and C-100. Instead there is clearly a synergistic effect in C-10 hybrid MOF exposing more active sites, deeper access of the electrode material to the electrolyte, and better charge transport together causing enhanced specific capacitance. The value of specific capacitance calculated for the C-10 composite was compared to the specific capacitance reported previously for other MOFs, their composites, and materials derived from MOFs based on Ni, Mn, Zr, Fe, Cu, Co, and Al, as can be seen in **Table 2** [51-60].

3.3. Performance of the electrode materials in a symmetric two-electrode system

Further, to assess the practical performance of the different MIL-53(Al)@rGO based materials, they were tested in a symmetric two-electrode system with each working electrode of 1 cm² dimension and mass loading of ~2 mg. The comparative CV and GCD curves (**Figure 8A** and **B**) show that the maximum specific capacitance was obtained for C-10, as indicated by the highest charging-discharging time and highest area under the CV loop (**Figure 8B**). The specific capacitance of the symmetric system using C-10 composite is calculated to be 75 F g⁻¹, which is 37.5 times that of pristine C-1 (2 F g⁻¹) and 1.2 times as compared to the pure rGO (62 F g⁻¹) (**Figure 8C**).

In order to further check the reversibility and efficiency of the electrode materials, coulombic efficiency (η) of all the composites are calculated using Eq. 2 at various current densities. As can be seen in **Figure 8C**, the coulombic efficiency increases with increasing the current density for all electrode materials. Indeed, at higher current densities, the overpotential for unwanted side reactions is larger limiting the parasitic side reaction, resulting in increased reversibility of the electrochemical interactions [61, 62]. The highest coulombic efficiency of 96% was recorded for rGO at the highest current density of 10 A g⁻¹. With an increase in the

amount of MIL-53 (Al) in the composites, the coulombic efficiency decreased, most likely due to the increase of internal resistance, as determined from the Nyquist plots [63]. Yet, the coulombic efficiency for the C-10 composite is 87% at 10 A g⁻¹, which is much higher than that of pristine C-1 (67%).

The plots of the energy density vs. power density of the electrode materials at various current densities (Ragone plots) are displayed in Figure 8D. An energy density of 6.66 Wh kg⁻¹ is attained for C-10 composite corresponding to a power density of 200 W kg⁻¹ at 0.5 A g⁻¹. Even at 3655 W kg⁻¹ (10 A g⁻¹), a retention of 2.75 Wh kg⁻¹ is obtained. This indicates the large power density range that can be achieved while maintaining a relatively high energy density for this composite. The enhancement in the energy density value is attributed to the optimum synergy availed at this particular concentration of rGO and MIL-53 (Al). Though rGO exhibits a very large surface area, only a very small fraction could be practically accessed by the electrolytic ions due to intense agglomeration and stacking of the sheets [64]. Integration of MIL-53 (Al) limits the stacking of the sheets to some extent, facilitating access of the electrolytic ions into the layers. Also, the bulk electrolytic interaction attributed to the presence of MIL-53 (Al) with a balanced internal resistance adds further to the enhanced performance of C-10 hybrid composite. Figure 8D also includes the Ragone plots projecting the energy and power densities reported previously for other MOF-based materials. As compared to other MOF-based electrode materials, such as Cu-CAT NW[55], NNPC-800 [65], MOF-5 [66], HCN-650 [67], Mn-MOF [51], the performance of the hybrid composite C-10 appears to be satisfactory.

Furthermore, to study the internal resistance, charge transfer kinetics, and ion diffusion characteristics, electrochemical impedance spectroscopic (EIS) measurements at open circuit potential in the frequency range of 100 kHz- 0.1 Hz were recorded. The Nyquist plots

(**Figure S4**) comprise a semicircular portion in the high frequency regime and a linear part in the lower frequency regime. The first intercept on the X-axis relates to series resistance (R_s) including the internal resistance by the electrode, interfacial contact resistance between the current collector and the electroactive material, and the electrolytic solution resistance. As can be seen from the magnified high frequency region (inset), the lowest intercept occurs for C-50 composite and the intercept value increases with decreasing the content of rGO towards C-2 hybrid composite with least amount of rGO and finally pristine MIL-53 (Al). The values of R_s of the synthesized samples are summarized in **Table 3**. The R_s value of pristine rGO was even greater, which could be attributed to the higher interfacial resistance and also interlayer resistance to the charge conduction. The integration of MIL-53 (Al) into the rGO led to intervening channels for electrolytic ion flow, reducing the resistance within the electrode material. Also, the wettability of the composite electrode surface towards the electrolyte is expected to increase due to the incorporation of MIL-53 (Al) into rGO promoting electrode-electrolyte interactions and hence causing a reduction of the interfacial resistance [68]. For the C-50 hybrid composite, the more vertical nature of the linear graph in the lower frequency region indicates lower ion diffusion resistance attributed to greater content of rGO [67].

The stability of the C-10 hybrid composite material was evaluated by running consecutive GCD measurements for 5,000 cycles at a current density of 3 A g^{-1} . As can be seen in **Figure 8E**, a sharp fall of the specific capacitance (about 30%) occurs at the end of 1,000 cycles. After 1,000 cycles, the electrode shows much stable characteristics (only 10% further reduction) for the next 3,000 cycles, retaining 60% of the initial capacitance at the end of 4,000 cycles. The electrode displays a rapid reduction in the specific capacitance thereafter retaining 50% of the initial specific capacitance after 5000 cycles.

4. Conclusion

In conclusion, MIL-53 (Al) (C-1) was synthesized through facile solvothermal method and further integrated with rGO to improve its electrical conductivity. The composite with 10% rGO content showed the most promising supercapacitive behavior with a specific capacitance of 280 F g⁻¹ at a current density of 0.5 A g⁻¹. The enhancement in the charge storage properties was attributed to established synergy between the MIL-53 (Al) MOF and rGO. The improved electrical conductivity and specific surface area, creation of shorter ion diffusion path and hierarchical pore features in the hybrid composite led to better charge storage properties, as compared to both rGO (C-100) and MIL-53 (Al) (C-1). The formed macropores in the hybrid composite can act as ion buffer reservoirs, while micropores provide high surface area; mesopores are favorable for creation of alternating pathways for ion diffusion within the electrode material. Furthermore, integration of rGO and MIL-53 (Al) resulted in elimination of the problem of agglomeration for both parent materials, exposing more active sites for electrode-electrolyte interactions. It is noteworthy that the performance of the hybrid composite (C-10) was not a mere addition of the performance from the parent materials, but was influenced by the established synergy and modified morphology unique to C-10. These results indicate the possibility of designing composites with better electrochemical performance from integration of carbon materials with pristine MOFs.

ASSOCIATED CONTENT

Supporting Information. TEM images; Cyclic voltammetry plots; Galvanostatic charge/discharge plots; Nyquist plots ([PDF](#)).

Acknowledgments

M.M. acknowledges Centre Franco-Indien pour la Promotion de la Recherche Avancée (CEFIPRA) and Campus France for support with fellowship under the Raman-Charpak Fellowship scheme. M. M. also acknowledges financial support from IIT (ISM), Dhanbad.

S.S. and R.B. acknowledge financial support from the Centre National de la Recherche Scientifique (CNRS) and University of Lille.

References

- [1] Y. Zhong, X. Cao, L. Ying, L. Cui, C. Barrow, W. Yang, J. Liu, Homogeneous nickel metal-organic framework microspheres on reduced graphene oxide as novel electrode material for supercapacitors with outstanding performance, *J. Colloid Interf. Sci.* 561 (2020) 265-274.
- [2] Q. Wang, J. Yan, Z. Fan, Carbon materials for high volumetric performance supercapacitors: design, progress, challenges and opportunities, *Energy Environ. Sci.* 9 (2016) 729-762.
- [3] V. B. Mohan, R. Brown, K. Jayaraman, D. Bhattacharyya, Characterisation of reduced graphene oxide: Effects of reduction variables on electrical conductivity, *Mater. Sci. Eng. B* 193 (2015) 49-60.
- [4] Z. Li, S. Gadipelli, Y. Yang, G. He, J. Guo, J. Li, Y. Lu, C.A. Howard, D.J.L. Brett, I.P. Parkin, F. Li, Z. Guo, Exceptional supercapacitor performance from optimized oxidation of graphene-oxide, *Energy Storage Mater.* 17 (2019) 12-21.
- [5] B. D. Ossoinon, D. Bélanger, Synthesis and characterization of sulfophenyl-functionalized reduced graphene oxide sheets, *RSC Adv.* 7 (2017) 27224-27234.
- [6] C. Dong, Y. Yu, X. Zhang, L. Huang, Y. Wu, J. Li, Z. Liu, An ionic liquid-modified reduced graphene oxide electrode material with favourable electrochemical properties, *New J. Chem.* 44 (2020) 6428-6434.
- [7] T. Zhao, S. Zhang, Y. Guo, Q. Wang, TiC₂: A new two-dimensional sheet beyond MXenes, *Nanoscale* 8 (2016) 233-242.
- [8] V.K.A. Muniraj, R. Boukherroub, M.V. Shelke, Flexible energy storage device based on Poly(N-phenylglycine), an incentive-energy pseudocapacitive conducting polymer, and electrochemically exfoliated graphite sheets, *ACS Sustain. Chem. Eng.* 8 (2020) 6433–6441.

- [9] Q. Pan, C. Duan, H. Liu, M. Li, Z. Zhao, D. Zhao, Y. Duan, Y. Chen, Y. Wang, Hierarchical vertically aligned titanium carbide (MXene) array for flexible all-solid-state supercapacitor with high volumetric capacitance, *ACS Appl. Energy Mater.* 2 (2019) 6834-6840.
- [10] D. Li, D. Zhu, W. Zhou, Q. Zhou, T. Wang, G. Ye, L. Lv, J. Xu, Design and electrosynthesis of monolayered MoS₂ and BF₄⁻-doped poly(3,4-ethylenedioxythiophene) nanocomposites for enhanced supercapacitive performance, *J. Electroanal. Chem.* 801 (2017) 345-353.
- [11] Y. Gawli, A. Banerjee, D. Dhakras, M. Deo, D. Bulani, P. Wadgaonkar, M. Shelke, S. Ogale, 3D polyaniline architecture by concurrent inorganic and organic acid doping for superior and robust high rate supercapacitor performance, *Sci. Rep.* 6 (2016) 21002-21012.
- [12] J. P. Zhu, X. H. Wang, X. X. Zuo, The application of metal-organic frameworks in electrode materials for Lithium-ion and Lithium-sulfur batteries, *R. Soc. Open Sci.* 6 (2019) 190634-190634.
- [13] R. Ramachandran, C. Zhao, D. Luo, K. Wang, F. Wang, Morphology-dependent electrochemical properties of cobalt-based metal organic frameworks for supercapacitor electrode materials, *Electrochim. Acta* 267 (2018) 170-180.
- [14] Y. Wang, S. Nie, Y. Liu, W. Yan, S. Lin, G. Cheng, H. Yang, J. Luo, Room-temperature fabrication of a nickel-functionalized copper metal-organic framework (Ni@Cu-MOF) as a new pseudocapacitive material for asymmetric supercapacitors, *Polymers* 11 (2019) 821-831.
- [15] K.M. Choi, H.M. Jeong, J.H. Park, Y.-B. Zhang, J.K. Kang, O.M. Yaghi, Supercapacitors of nanocrystalline metal-organic frameworks, *ACS Nano* 8 (2014) 7451-7457.
- [16] R. Díaz, M.G. Orcajo, J.A. Botas, G. Calleja, J. Palma, Co⁸-MOF-5 as electrode for supercapacitors, *Mater. Lett.* 68 (2012) 126-128.
- [17] J. Yang, Z. Ma, W. Gao, M. Wei, Layered structural Co-based MOF with conductive network frames as a new supercapacitor electrode, *Chem. Eur. J.* 23 (2017) 631-636.

- [18] J. Yang, P. Xiong, C. Zheng, H. Qiu, M. Wei, Metal–organic frameworks: A new promising class of materials for a high performance supercapacitor electrode, *J. Mater. Chem. A* 2 (2014) 16640-16644.
- [19] Y. Xu, Q. Li, H. Xue, H. Pang, Metal-organic frameworks for direct electrochemical applications, *Coord. Chem. Rev.* 376 (2018) 292-318.
- [20] W. Jiang, J. Pan, X. Liu, A novel rod-like porous carbon with ordered hierarchical pore structure prepared from Al-based metal-organic framework without template as greatly enhanced performance for supercapacitor, *J. Power Sources* 409 (2019) 13-23.
- [21] W. Jiang, J. Cai, J. Pan, S. Guo, Y. Sun, L. Li, X. Liu, Nitrogen-doped hierarchically ellipsoidal porous carbon derived from Al-based metal-organic framework with enhanced specific capacitance and rate capability for high performance supercapacitors, *J. Power Sources* 432 (2019) 102-111.
- [22] N. Tannert, C. Jansen, S. Nießing, C. Janiak, Robust synthesis routes and porosity of the Al-based metal–organic frameworks Al-fumarate, CAU-10-H and MIL-160, *Dalton Trans.* 48 (2019) 2967-2976.
- [23] H. Li, X. Feng, D. Ma, M. Zhang, Y. Zhang, Y. Liu, J. Zhang, B. Wang, Stable aluminum metal–organic frameworks (Al-MOFs) for balanced CO₂ and water selectivity, *ACS Appl. Mater. Interfaces* 10 (2018) 3160-3163.
- [24] X. Qian, B. Yadian, R. Wu, Y. Long, K. Zhou, B. Zhu, Y. Huang, Structure stability of metal-organic framework MIL-53 (Al) in aqueous solutions, *Int. J. Hydrogen Energy* 38 (2013) 16710-16715.
- [25] M. S. Sánchez, N. Getachew, K. Díaz, M. D. García, Y. Chebude, I. Díaz, Synthesis of metal–organic frameworks in water at room temperature: salts as linker sources, *Green Chem.* 17 (2015) 1500-1509.
- [26] S. Nießing, C. Janiak, Studies on catalytic activity of MIL-53(Al) and structure analogue DUT-5(Al) using bdc- and bpdc-ligands functionalized with L-proline in a solid-solution mixed-linker approach, *Mol. Catal.* 467 (2019) 70-77.

- [27] A. Sharma, J. K. Bhattarai, S. S. Nigudkar, S. G. Pistorio, A. V. Demchenko, K. J. Stine, Electrochemical impedance spectroscopy study of carbohydrate-terminated alkanethiol monolayers on nanoporous gold: Implications for pore wetting, *J. Electroanal. Chem.* 782 (2016) 174-181.
- [28] K. W. Knehr, T. Hodson, C. Bommier, G. Davies, A. Kim, D. A. Steingart, Understanding Full-cell evolution and non-chemical electrode crosstalk of Li-ion batteries, *Joule* 2 (2018) 1146-1159.
- [29] Y. Wang, W. Lai, N. Wang, Z. Jiang, X. Wang, P. Zou, Z. Lin, H. J. Fan, F. Kang, C. P. Wong, C. Yang, A reduced graphene oxide/mixed-valence manganese oxide composite electrode for tailorable and surface mountable supercapacitors with high capacitance and super-long life, *Energy Environ. Sci.* 10 (2017) 941-949.
- [30] M. Majumder, R. B. Choudhary, A. K. Thakur, Hemispherical nitrogen-doped carbon spheres integrated with polyindole as high performance electrode material for supercapacitor applications, *Carbon* 142 (2019) 650-661.
- [31] B. Sun, H. Tan, S. Liu, S. Lyu, X. Zhang, Y. Zhang, J. Li, L. Wang, Novel cobalt catalysts supported on metal-organic frameworks MIL-53(Al) for the Fischer-Tropsch synthesis, *Energy Technol.* 7 (2019) 1800802.
- [32] K. Zhang, Y. Zhang, S. Wang, Enhancing thermoelectric properties of organic composites through hierarchical nanostructures, *Sci. Rep.* 3 (2013) 3448.
- [33] J. F. Liu, J. C. Mu, R. X. Qin, S. F. Ji, Pd nanoparticles immobilized on MIL-53(Al) as highly effective bifunctional catalysts for oxidation of liquid methanol to methyl formate, *Petroleum Sci.* 16 (2019) 901-911.
- [34] R. M. Olivan, M. J. Cocero, J. Coronas, S. R. Rojo, Supercritical CO₂ encapsulation of bioactive molecules in carboxylate based MOFs, *J. CO₂ Util.* 30 (2019) 38-47.
- [35] F. T. Johra, W. G. Jung, Hydrothermally reduced graphene oxide as a supercapacitor, *Appl. Surf. Sci.* 357 (2015) 1911-1914.

- [36] P. Rallapalli, K. P. Prasanth, D. Patil, R. S. Somani, R. V. Jasra, H. C. Bajaj, Sorption studies of CO₂, CH₄, N₂, CO, O₂ and Ar on nanoporous aluminum terephthalate [MIL-53(Al)], *J. Porous Mater.* 18 (2011) 205-210.
- [37] J. H. Lee, S. Jeoung, Y. G. Chung, H. R. Moon, Elucidation of flexible metal-organic frameworks: Research progresses and recent developments, *Coord. Chem. Rev.* 389 (2019) 161-188.
- [38] A. E. J. Hoffman, L. Vanduyfhuys, I. Nevjestić, J. Wieme, S. M. J. Rogge, H. Depauw, P. Van Der Voort, H. Vrielinck, V. Van Speybroeck, Elucidating the Vibrational Fingerprint of the flexible metal-organic framework MIL-53(Al) using a combined experimental/computational approach, *J. Phys. Chem. C* 122 (2018) 2734-2746.
- [39] T. Loiseau, C. Serre, C. Huguenard, G. Fink, F. Taulelle, M. Henry, T. Bataille, G. Férey, A rationale for the large breathing of the porous aluminum terephthalate (MIL-53) upon hydration, *Chem. Eur. J* 10 (2004) 1373-1382.
- [40] A. Schneemann, V. Bon, I. Schwedler, I. Senkovska, S. Kaskel, R.A. Fischer, Flexible metal-organic frameworks, *Chem. Soc. Rev.* 43 (2014) 6062-6096.
- [41] C. Li, L. Zhu, W. Yang, X. He, S. Zhao, X. Zhang, W. Tang, J. Wang, T. Yue, Z. Li, Amino-functionalized Al-MOF for fluorescent detection of tetracyclines in milk, *J. Agric. Food Chem.* 67 (2019) 1277-1283.
- [42] J. Zhang, Y. Xu, Z. Liu, W. Yang, J. Liu, A highly conductive porous graphene electrode prepared via in situ reduction of graphene oxide using Cu nanoparticles for the fabrication of high performance supercapacitors, *RSC Adv.* 5 (2015) 54275-54282.
- [43] C. M. Moran, J. N. Joshi, R. M. Marti, S. E. Hayes, K. S. Walton, Structured growth of metal-organic framework MIL-53(Al) from solid aluminum carbide precursor, *J. Am. Chem. Soc.* 140 (2018) 9148-9153.
- [44] R. Sadri, M. Hosseini, S.N. Kazi, S. Bagheri, N. Zubir, K.H. Solangi, T. Zaharinie, A. Badarudin, A bio-based, facile approach for the preparation of covalently functionalized carbon nanotubes aqueous suspensions and their potential as heat transfer fluids, *J. Colloid Interface Sci.* 504 (2017) 115-123.

- [45] S. G. Menon, K. S. Choudhari, S. A. Shivashankar, S. Chidangil, S. D. Kulkarni, Microwave solution route to ceramic ZnAl_2O_4 nanoparticles in 10 minutes: inversion and photophysical changes with thermal history, *New J. Chem.* 41 (2017) 5420-5428.
- [46] K. A. Cychoz, R. Guillet-Nicolas, J. García-Martínez, M. Thommes, Recent advances in the textural characterization of hierarchically structured nanoporous materials, *Chem. Soc. Rev.* 46 (2017) 389-414.
- [47] E. Rahmani, M. Rahmani, Al-based MIL-53 metal organic framework (mof) as the new catalyst for Friedel–Crafts alkylation of benzene, *Ind. Eng. Chem. Res.* 57 (2018) 169-178.
- [48] V. K. A. Muniraj, P. K. Dwivedi, P. S. Tamhane, S. Szunerits, R. Boukherroub, M. V. Shelke, High-energy flexible supercapacitor—synergistic effects of polyhydroquinone and $\text{RuO}_2 \cdot x\text{H}_2\text{O}$ with microsized, few-layered, self-supportive exfoliated-graphite sheets, *ACS Appl. Mater. Interfaces* 11 (2019) 18349-18360.
- [49] B. Pandit, D.P. Dubal, B.R. Sankapal, Large scale flexible solid state symmetric supercapacitor through inexpensive solution processed V_2O_5 complex surface architecture, *Electrochim. Acta* 242 (2017) 382-389.
- [50] Y.A. Ismail, J. Chang, S.R. Shin, R.S. Mane, S.-H. Han, S.J. Kim, Hydrogel-assisted polyaniline microfiber as controllable electrochemical actuatable supercapacitor, *J. Electrochem. Soc.* 156 (2009) A313.
- [51] Y. Zhang, B. Lin, Y. Sun, X. Zhang, H. Yang, J. Wang, Carbon nanotubes@metal–organic frameworks as Mn-based symmetrical supercapacitor electrodes for enhanced charge storage, *RSC Adv.* 5 (2015) 58100-58106.
- [52] W. Gao, D. Chen, H. Quan, R. Zou, W. Wang, X. Luo, L. Guo, Fabrication of Hierarchical Porous Metal–Organic Framework Electrode for Aqueous Asymmetric Supercapacitor, *ACS Sustain. Chem. Eng.* 5 (2017) 4144-4153.
- [53] A. Farisabadi, M. Moradi, S. Borhani, S. Hajati, M.A. Kiani, S.A. Tayebifard, Synthesis and electrochemical properties of Mg-doped chromium-based metal organic framework/reduced graphene oxide composite for supercapacitor application, *J. Mater. Sci.: Mater. Electron.* 29 (2018) 8421-8430.

- [54] H. Wang, Z. Huang, H. Zhao, F. Zhang, C. Xu, Q. Fu, H. Tao, H. Li, J. Ma, Electrochemical performance of $\text{Fe}_x\text{Mn}_{1-x}$ -based metal–organic frameworks as electrode materials for supercapacitors, *J. Mater. Sci.: Mater. Electron.* 29 (2018) 19819-19824.
- [55] W. H. Li, K. Ding, H.-R. Tian, M. S. Yao, B. Nath, W. H. Deng, Y. Wang, G. Xu, Conductive Metal–Organic Framework Nanowire Array Electrodes for High-Performance Solid-State Supercapacitors, *Adv. Funct. Mater.* 27 (2017) 1702067.
- [56] D. Y. Lee, S. J. Yoon, N. K. Shrestha, S. H. Lee, H. Ahn, S. H. Han, Unusual energy storage and charge retention in Co-based metal–organic-frameworks, *Microporous Mesoporous Mater.* 153 (2012) 163-165.
- [57] D. Zhu, H. Li, Y. Su, M. Jiang, Pyridine-containing metal-organic frameworks as precursor for nitrogen-doped porous carbons with high-performance capacitive behavior, *J. Solid State Electrochem.* 21 (2017) 2037-2045.
- [58] R. Ramachandran, C. Zhao, D. Luo, K. Wang, F. Wang, Synthesis of copper benzene-1, 3, 5-tricarboxylate metal organic frameworks with mixed phases as the electrode material for supercapacitor applications, *Appl. Surf. Sci.* 460 (2018) 33-39.
- [59] S. Zhang, X. Shi, D. Moszyński, T. Tang, P.K. Chu, X. Chen, E. Mijowska, Hierarchical porous carbon materials from nanosized metal-organic complex for high-performance symmetrical supercapacitor, *Electrochim. Acta* 269 (2018) 580-589.
- [60] B. Guo, Y. Yang, Z. Hu, Y. An, Q. Zhang, X. Yang, X. Wang, H. Wu, Redox-active organic molecules functionalized nitrogen-doped porous carbon derived from metal-organic framework as electrode materials for supercapacitor, *Electrochim. Acta* 223 (2017) 74-84.
- [61] A. K. Thakur, M. Majumder, R. B. Choudhary, S.B. Singh, MoS_2 flakes integrated with boron and nitrogen-doped carbon: Striking gravimetric and volumetric capacitive performance for supercapacitor applications, *J. Power Sources* 402 (2018) 163-173.
- [62] T. Chen, Y. Tang, Y. Qiao, Z. Liu, W. Guo, J. Song, S. Mu, S. Yu, Y. Zhao, F. Gao, All-solid-state high performance asymmetric supercapacitors based on novel MnS nanocrystal and activated carbon materials, *Sci. Rep.* 6 (2016) 23289.

- [63] S. He, X. Hu, S. Chen, H. Hu, M. Hanif, H. Hou, Needle-like polyaniline nanowires on graphite nanofibers: hierarchical micro/nano-architecture for high performance supercapacitors, *J. Mater. Chem.* 22 (2012) 5114-5120.
- [64] Q. Cheng, J. Tang, N. Shinya, L.-C. Qin, Polyaniline modified graphene and carbon nanotube composite electrode for asymmetric supercapacitors of high energy density, *J. Power Sources* 241 (2013) 423-428.
- [65] J. Zou, P. Liu, L. Huang, Q. Zhang, T. Lan, S. Zeng, X. Zeng, L. Yu, S. Liu, H. Wu, W. Tu, Y. Yao, Ultrahigh-content nitrogen-decorated nanoporous carbon derived from metal organic frameworks and its application in supercapacitors, *Electrochim. Acta* 271 (2018) 599-607.
- [66] L. Wang, T. Wei, L. Sheng, L. Jiang, X. Wu, Q. Zhou, B. Yuan, J. Yue, Z. Liu, Z. Fan, “Brick-and-mortar” sandwiched porous carbon building constructed by metal-organic framework and graphene: Ultrafast charge/discharge rate up to 2 V s^{-1} for supercapacitors, *Nano Energy* 30 (2016) 84-92.
- [67] T. Gao, F. Zhou, W. Ma, H. Li, Metal-organic-framework derived carbon polyhedron and carbon nanotube hybrids as electrode for electrochemical supercapacitor and capacitive deionization, *Electrochim. Acta* 263 (2018) 85-93.
- [68] P. Wen, P. Gong, J. Sun, J. Wang, S. Yang, Design and synthesis of Ni-MOF/CNT composites and rGO/carbon nitride composites for an asymmetric supercapacitor with high energy and power density, *J. Mater. Chem. A* 3 (2015) 13874-13883.

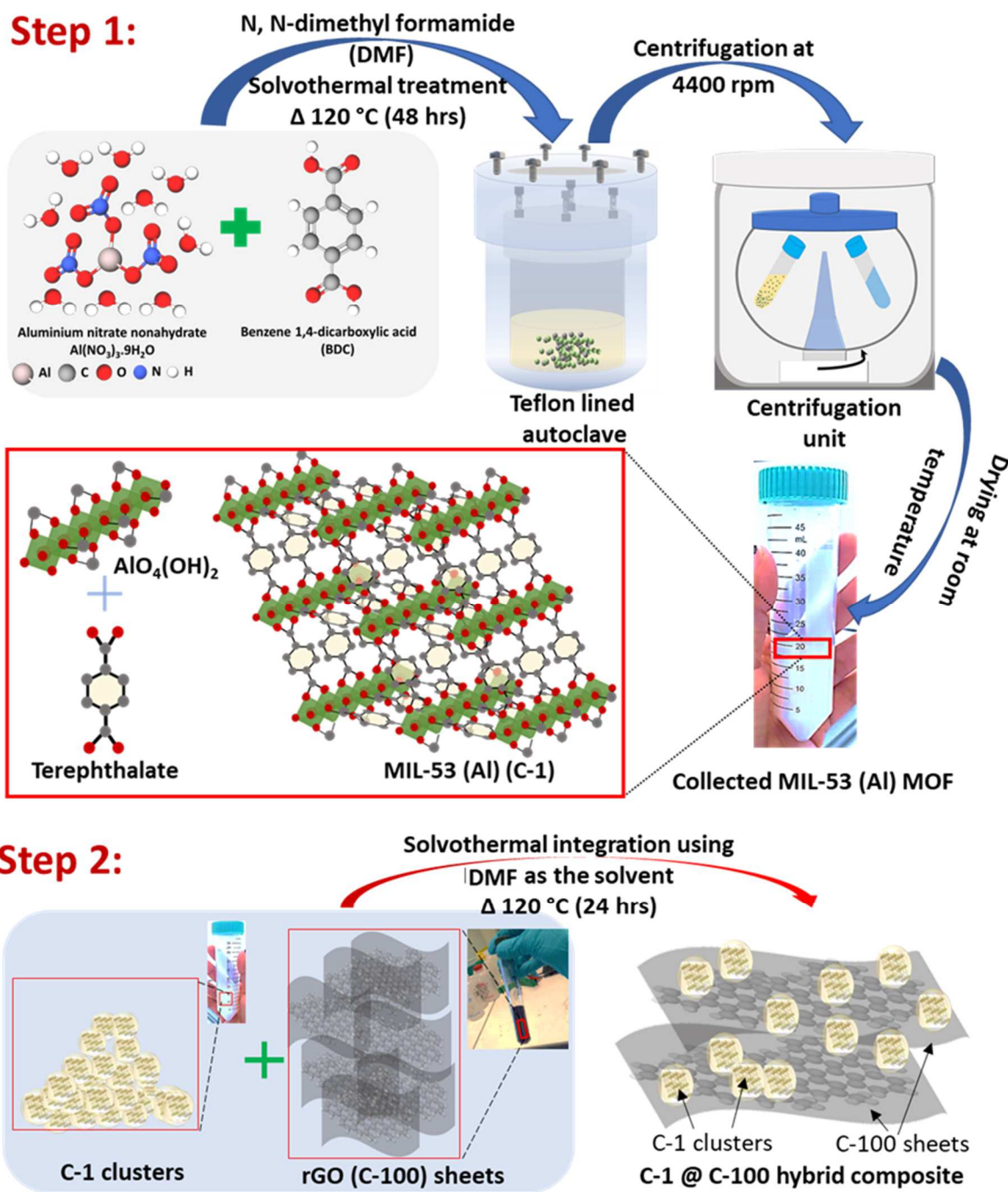


Figure 1. Step1: Schematic of synthetic route of MIL-53 (Al) (C-1) and structure of C-1 metal-organic framework showing the bridging terephthalate molecules to the octahedral units of $\text{AlO}_4(\text{OH})_2$; Step 2: solvothermal integration of C-1 and reduced graphene oxide (rGO).

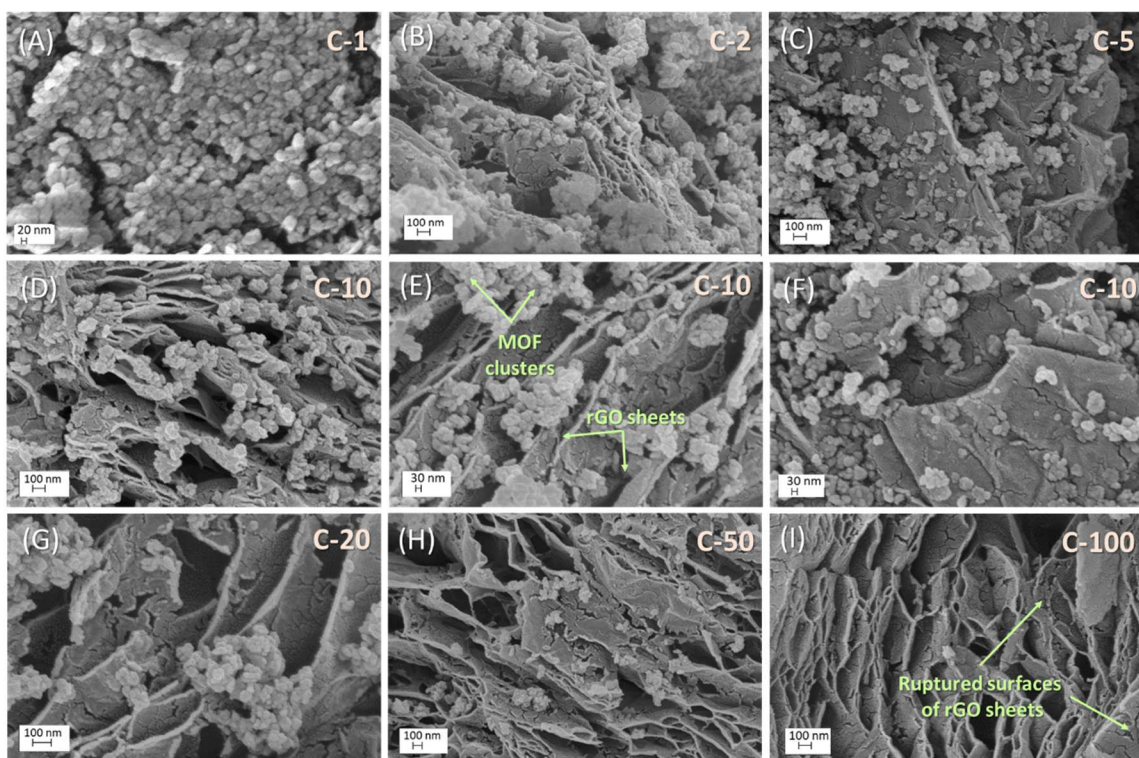


Figure 2. FE-SEM images of (A) pristine MOF C-1, and (B) C-2, (C) C-5, (D-F) C-10 (G) C-20, (H) C-50, and (I) C-100 hybrid composites at various magnifications.

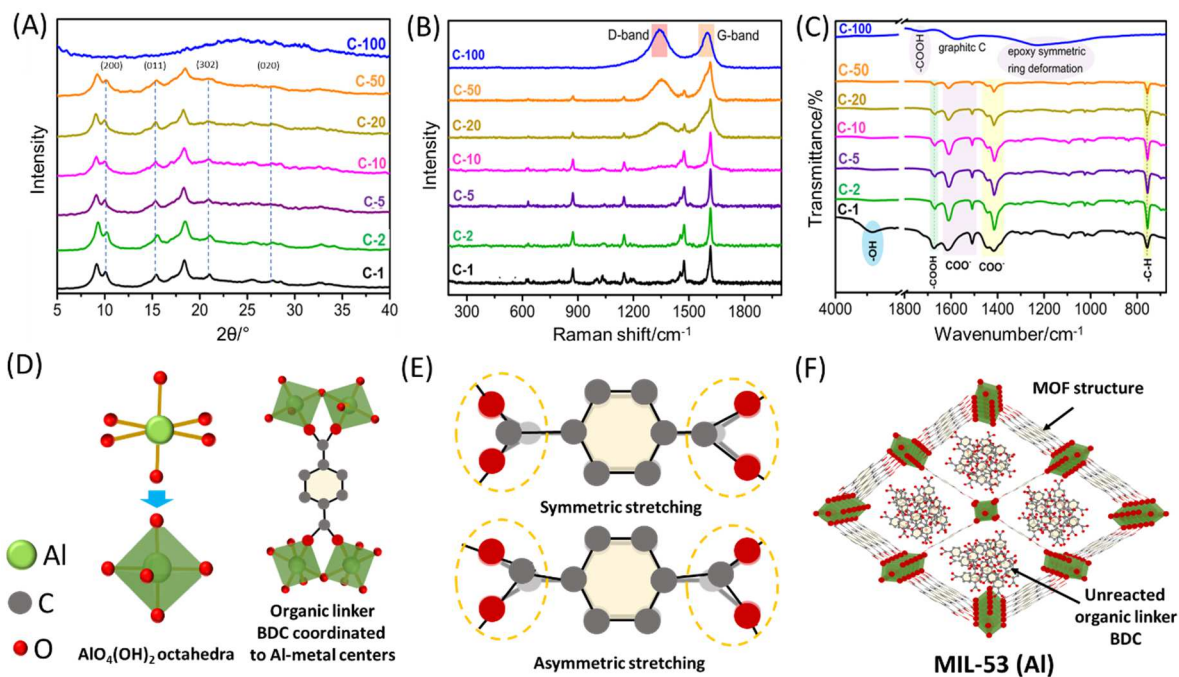


Figure 3. Characterization of MIL-53 (Al) and MIL-53 (Al)@rGO hybrid composite electrode materials: (A) XRD patterns, (B) Raman spectra, (C) FTIR spectra, (D) Al-atom coordination bonds with six other oxygen atoms to form the $\text{AlO}_4(\text{OH})_2$ octahedra, (E) symmetric and asymmetric stretching of the $-\text{COO}^-$ coordinated to Al-metal cluster belonging to organic linker BDC, (F) trapped unreacted molecules of organic linker BDC within the pores of MOF.

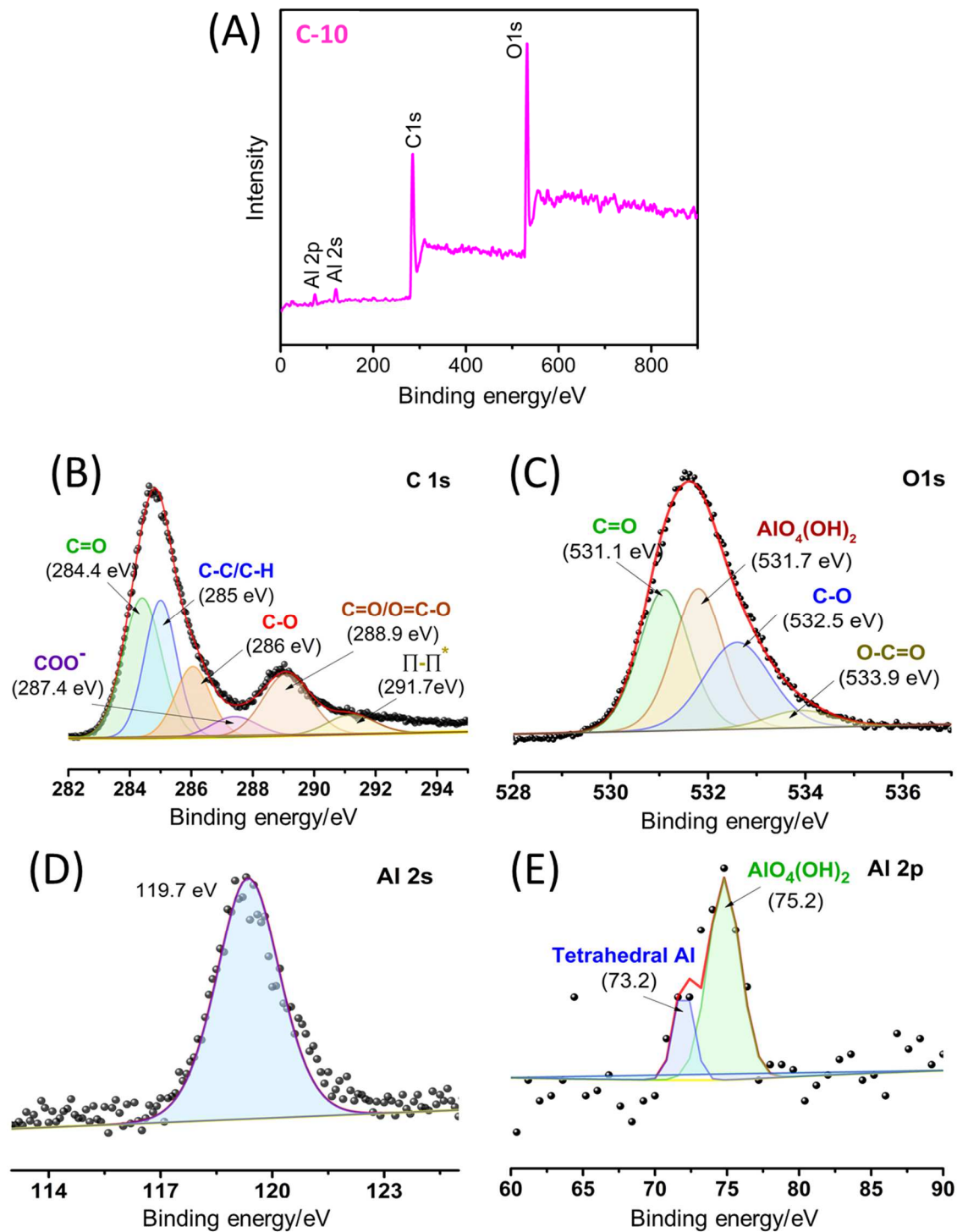


Figure 4. X-ray photoelectron analysis of C-10: (A) XPS survey scan, and core level spectra of (B) C 1s, (C) O 1s, (D) Al 2s, and (E) Al 2p.

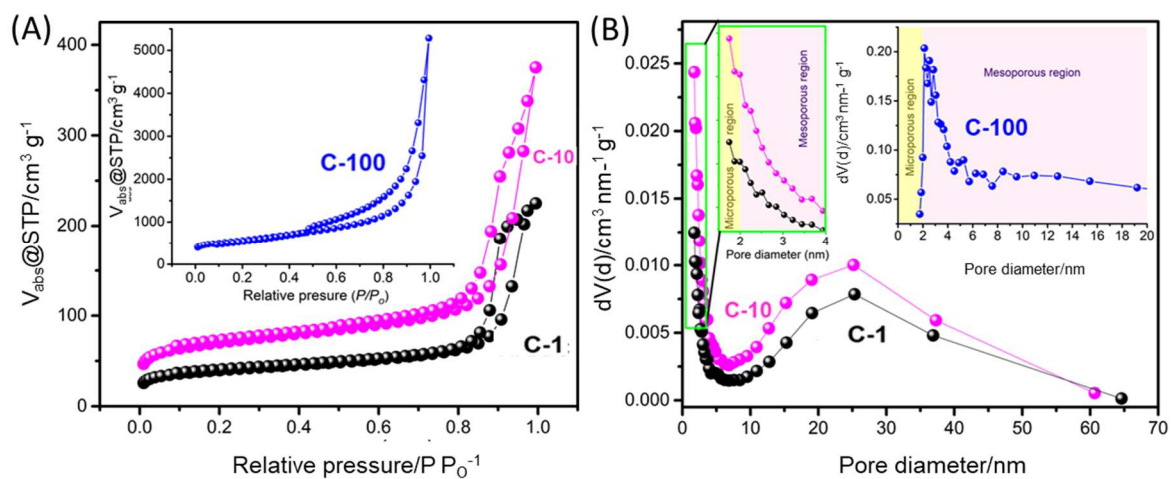


Figure 5. (A) N₂ adsorption-desorption isotherms, and (B) BJH pore size distribution of C-1, C-10 and C-100 (inset) composites.

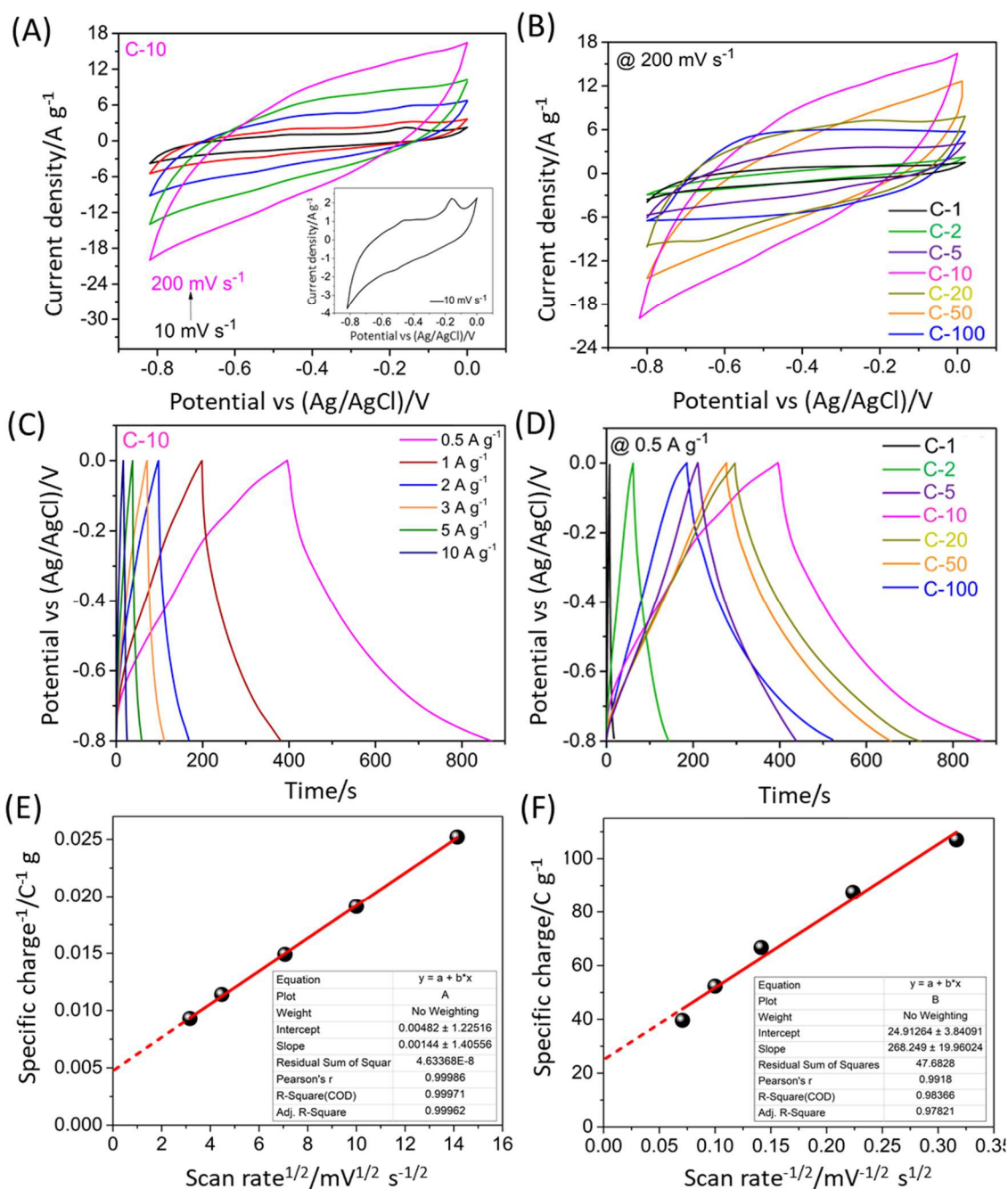


Figure 6. (A) Cyclic voltammetry profiles of different MIL-53 (Al)@rGO electrodes at room temperature in 1 M KOH aqueous solution. (B) Comparative cyclic voltammetry plots of all the electrode materials. (C) Charge-discharge curves of C-10 in 1 M KOH at various current densities. (D) Comparison of charge-discharge curves of the different MIL-53 (Al)@rGO electrodes at 0.5 A g⁻¹. (E) q^{-1} vs. scan rate^{1/2} plot of C-10 hybrid composite. (F) q vs. scan rate^{-1/2} plot of C-10 hybrid composite.

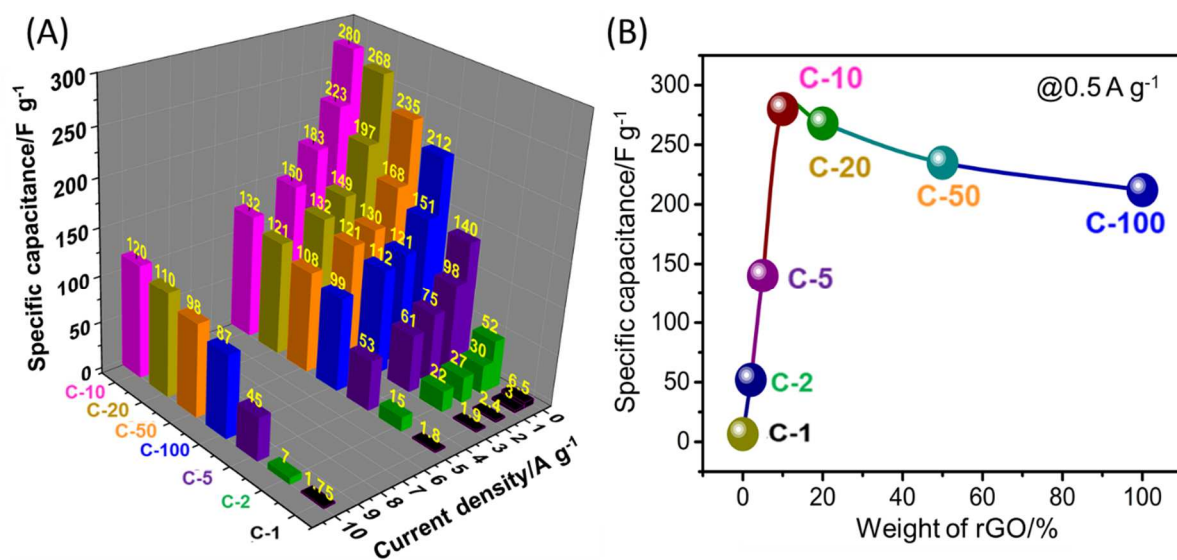


Figure 7. (A) Specific capacitance as calculated from the discharging time for the electrode materials. (B) The variation of the specific capacitance values obtained at 0.5 A g⁻¹ with the varying content of rGO in the composites.

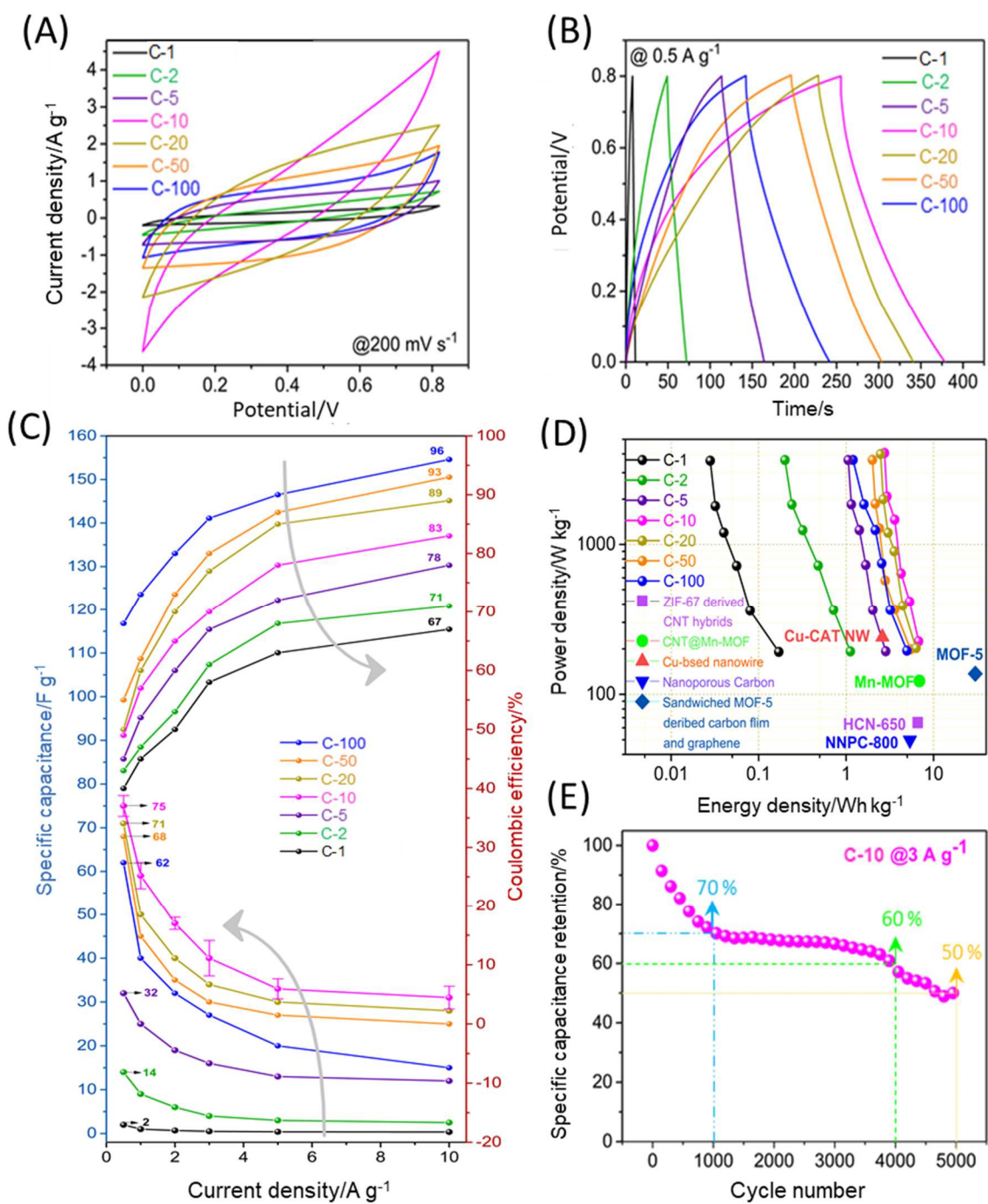


Figure 8. (A) Comparative cyclic voltammety plots. (B) Comparative galvanostatic charging/discharging curves. (C) Variation of the coulombic efficiency and the specific capacitance at various applied currents. (D) Ragone plots of the synthesized electrode materials. (E) Cyclic stability of C-10 composite.

Table 1. Formation of different of MIL-53 (Al)@rGO nanocomposites by varying the ratio of MIL-53 (Al) and rGO.

MIL-53 (Al) @rGO	rGO/wt%	MIL-53 (Al)/wt%
C-1	0	100
C-2	2	98
C-5	5	95
C-10	10	90
C-20	20	80
C-50	50	50
C-100	100	0

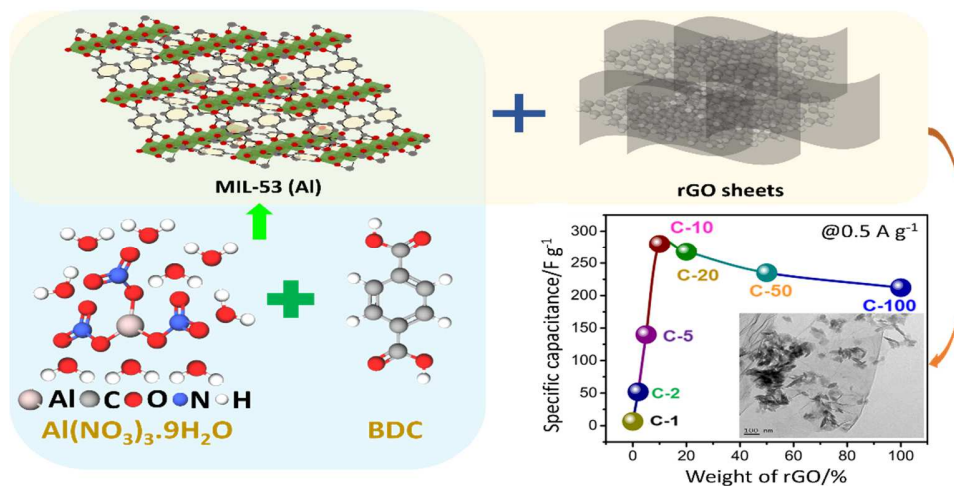
Table 2. Specific capacitance obtained for other MOFs and MOF-derived materials and their composites.

Sample	Electrolyte	Current density/A g ⁻¹	Specific capacitance /F g ⁻¹	Ref.
Mn-MOF	1 M Na ₂ SO ₄	1	28.4	[51]
Zr-MOF (UiO-66)	6 M KOH	0.2	101.5	[52]
Cr-based MOF composite with rGO (MIL-101(Cr)/rGO)	6 M KOH	1	137.46	[53]
Fe doped Mn-MOF	1 M Na ₂ SO ₄	0.01	167.95	[54]
Conductive copper based MOF nanowire arrays (Cu-CAT NWAs)	3 M KCl	0.5	202.0	[55]
Composite of carbon nano tube and Mn-MOF	1 M Na ₂ SO ₄	1	202.8	[51]
Co-MOF	1 M LiOH	0.6	206.7	[56]
Pyridine-containing MOF derived N-doped porous carbon	6 M KOH	1	226.6	[57]
Copper benzene@1, 3, 5-tricarboxylate MOF	3 M KOH	1.5	228	[58]
Nano porous carbon prepared from Al-MOF (NPC -50)	1 M H ₂ SO ₄	1	249.0	[59]
Nanoporous carbon derived from ZIF-8	1 M H ₂ SO ₄	1	254.0	[60]
Mg doped Cr-based MOF composite with rGO (MIL-101 (Cr,Mg)/rGO)	6 M KOH	1	261.41	[53]
MIL-53(Al)@rGO (C-10)	1 M KOH	0.5	280.0	This work

Table 3. Series resistance (R_s) values from Nyquist plots for the electrode materials.

Electrode material	Series resistance value R_s/Ω
C-1	3.05
C-2	2.89
C-5	2.83
C-10	2.70
C-20	2.50
C-50	2.30
C-100	4.54

Graphical Abstract



Hybrid composite of aluminum terephthalate MIL-53 (Al) with reduced graphene oxide synthesized through solvothermal approach exhibits enhanced electrochemical charge storage properties. The hybrid composite shows better pore features and modified morphology with lesser agglomeration. The hybrid composite also exhibits better charge conductivity.